# Strain Engineering of Wave-like Nanofibers for Dynamically Switchable Adhesive/Repulsive Surfaces

*William S. Y. Wong, Philipp Gutruf, Sharath Sriram, Madhu Bhaskaran, Zuankai Wang, and Antonio Tricoli\**

Engineering surfaces that enable the dynamic tuning of their wetting state is critical to many applications including integrated microfluidics systems, flexible electronics, and smart fabrics. Despite extensive progress, most of the switchable surfaces reported are based on ordered structures that suffer from poor scalability and high fabrication costs. Here, a robust and facile bottom-up approach is demonstrated that allows for the dynamical and reversible switching between lotus leaf (repulsive) and rose petal (adhesive) states by strain engineering of wave-like nanofiber layers. Interestingly, it is found that the controlled switching between these two distinctive states is sensitive to the shape of the nanofibers. Moreover, it is observed that the structural integrity of the nanofibers is fully preserved during multicycle dynamic switching. The application of these optimal structures is showcased as mechanical hands demonstrating the capture of water microdroplets and their subsequent release in a well-controlled manner. It is envisioned that this low-cost and highly scalable surface texture is a powerful platform for the design of portable microfluidics systems, and the fabrication of large-scale devices for ambient humidity harvesting and water purification.

## 1. Introduction

Development of novel multiscale materials with dynamically tunable[1] wetting states bears significant commercial potential. Their integration in fabrics[2] is a key step for the fabrication of smart[3,4] weather-adaptive materials, and of an increasing number of coatings utilized in tissue engineering,[5] microfluidics,[6,7] and drug delivery.[8] In particular, owing to their advantages of not requiring bulk peristaltic systems, dynamically switchable[1,9] superhydrophobic and hydrophilic surfaces[10,11] are a potential cornerstone of next generation microfluidics devices.[7,12] Recently, tunable[11] surfaces based on arrays of aligned nanopillars have been achieved by controlled shapeshifting of surface texturing and wettability.[8,13] However, the wide-spread utilization of such lithography-based ordered structures[14] is limited due to their limited scalability and high fabrication cost. Thus, the ability to achieve dynamic tuning of surface wetting with disordered morphologies is critical for their commercial application.

Strain-induced modification of the morphological features of a film such as wrinkling and buckling is a flexible actuation mechanism that is found in a multitude of scales in nature. These range from biocellular epidermal layers of skin[15] to geological wrinkles.[16] In synthetic processes, the spontaneous wrinkling of thin films[17] has traditionally been treated as a defect, with significant efforts directed toward the fabrication of perfectly flat surfaces.[18] Recently, artificial skin-like wrinkling materials have been proposed as a powerful multifunctional structure for several applications including flexible electronics,[19,20] self-assembling 3D architectures,[21,22] bioactive materials,[5,23] particle sieves,[15] and membrane technologies.[4,24] These multifunctional materials are commonly fabricated by deposition of flat 2D solid thin films such as silica,[15,23] gold,[5,25] carbon nanotubes,[26] graphene,[27] and thin polystyrene films[28] on prestretched elastomeric substrates. Relaxation of the prestretched substrate wrinkles the top film into a multiscale nano–micro rough hierarchical structure, with demonstrated potential for enabling tunable wettability.[5]

Here, we demonstrate an alternative concept to achieve dynamically reversible wetting from hydrophobic to superhydrophobic and switchable droplet adhesion/repulsion. Our method is based on the facile and scalable incorporation of polystyrene nanofiber layers on soft elastic substrates. By anisotropic stretching and self-relaxation of the elastic substrate, the originally 1D nanofibers are reversibly transformed into

W. S. Y. Wong, Dr. A. Tricoli
Nanotechnology Research Laboratory
Research School of Engineering
The Australian National University
Canberra ACT 2601, Australia
E-mail: antonio.tricoli@anu.edu.au
P. Gutruf, Dr. S. Sriram, Dr. M. Bhaskaran
Functional Materials and Microsystems Research Group and
Micro Nano Research Facility
RMIT University
Melbourne VIC 3001, Australia
Prof. Z. Wang
Department of Mechanical and Biomedical Engineering
City University of Hong Kong
Hong Kong 999077, China

wave-like 2D structures with a range of superhydrophobic wetting states. Continuous strain–relaxation cycles demonstrate fully reversible dynamic tuning of wettability and droplet adhesion between repulsive lotus leaf and adhesive rose petal states. Application of these optimal structures as mechanical hands is showcased by controlled capture, manipulation and release of microdroplets. This bottom-up design offers a flexible platform for the fabrication of tunable materials with applications including flexible microelectronics,[19] tissue engineering[5,29] and 3D self-assembly.[21]

## 2. Results and Discussion

ID polystyrene nanofibers were synthesized by scalable, low cost electrospinning of polymer solutions. The average fiber diameter measured by scanning electron microscopy (SEM) was 170 ± 55 nm. To fabricate 2D wave-like nanofibers, we electrospun the as-synthesized nanofibers directly on prestretched polydimethylsiloxane (PDMS) films (Figure S1,

Supporting Information) that were subjected to up to 100% mono- or biaxial prestretches. The as-prepared PDMS films (Figure S8, Supporting Information) had inherent contact angles of 119 ± 1.3°. In our experiments, three different arrangements of nanofibers relative to the prestretching direction were investigated, namely, parallel, orthogonally, and randomly aligned. **Figure 1**a shows the deposition of nanofibers parallel-aligned to the prestretching direction of the PDMS films. For these parallel-aligned fiber layers, relaxation of the PDMS substrate resulted in controlled compression of the nanofibers, leading to the assembly of in-plane and out-of-plane wave-like nanostructures (Figure 1a,b, and Figure S2a, Supporting Information). The two types of fibers were classified according to the orientation of their longitudinal axes. In-plane fibers have longitudinal axes that are parallel to the substrate while out-of-plane fibers have longitudinal axes that are partially perpendicular to the substrate. As a result, it was possible to identify these two types of fibers by SEM focal depth analysis and white light interferometry (WLI) (Figures S2a, S4, S5, and S7, Supporting Information). The relatively large amount
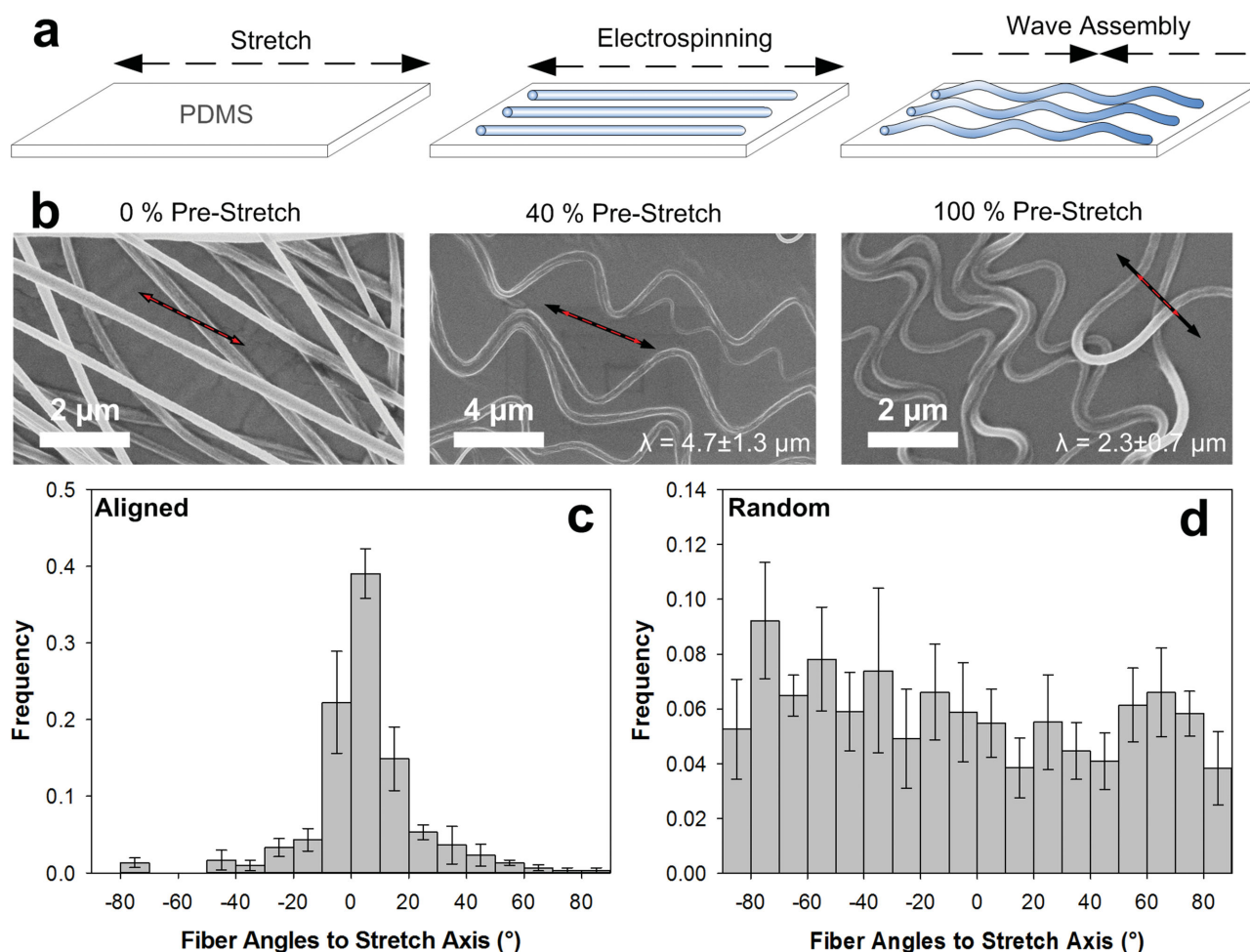


**Figure 1.** a) Schematic description of wave-like nanofiber synthesis by relaxation of electrospun layers of parallel-aligned nanofibers on prestretched substrates. b) Relaxation of the substrates gives rise to wave-like nanofibers with wavelengths of 4.7 ± 1.3 and 2.3 ± 0.7 μm at 40% and 100% prestretching, respectively. Black and red arrows indicate alignment direction and stretch-compression ratio, respectively. Histogram counts of fiber angle to prestretch axis for c) parallel and d) randomly aligned electrospinning of nanofibers. The error bars represent the standard errors amongst five different batches.

www.MaterialsViews.com

ADVANCED
FUNCTIONAL
MATERIALS
www.afm-journal.de

FULL PAPER

of in-plane fibers, obtained here over that observed for previous single layer[19] studies, is tentatively attributed both to the affinity of the PDMS substrate with the polystyrene nanofibers and the partial interweaving of the electrospun layers. These forces contribute to confine the vertical displacement of the bottom and lower nanofiber layers during compression resulting in a wave-like morphology. This assembly of in-plane and out-of-plane nanofibers possesses a corrugated, twisted surface[30] texture (Figure S2a, Supporting Information) that resembles the characteristic morphology of the superhydrophobic silver ragwort leaves.[30,31] The wavelengths of the in-plane fibers decreased from 4.7 ± 1.3 to 2.3 ± 0.74 µm with increasing prestretch from 40% to 100% (Figure 1b). The out-of-plane nanofibers had a nearly twice as large wavelength reaching 9.4 µm at 40% prestretch. The amount of these out-of-plane fibers was found to decrease with decreasing film thickness and optimal films were obtained with an electrodeposition time of 1 min having a lower number of vertically stock nanofiber layers. Longer deposition time (3 min) led to static repulsive lotus-like superhydrophobic surfaces that were, however, not tunable. This is attributed to the poor transmission of the substrate strain in such highly porous film structures. Assessment of the tunable films (1 min deposition) through WLI optical profiling reveal an average thickness of 4.8 µm with a SEM-determined effective surface coverage of 56 ± 9% (Figure S3, Supporting Information).

Orthogonally and randomly oriented nanofiber films were obtained as control structures by placing the counter electrodes on the matching orthogonal extremities and on the perimeter of whole PDMS films (Figure S1c, Supporting Information),

respectively. The orthogonally aligned fibers had an increased packing density but preserved the initial straight morphology (Figure S4a–c, Supporting Information). Randomly-aligned nanofibers had few wave-like structures and some closely-packed domains showing an intermediary state between the former two alignment orientations (Figure S5f, Supporting Information). Significantly less directional scattering was observed for the orthogonally aligned nanofibers than for the parallel-aligned ones (Figure S5a,b, Supporting Information). Statistical investigation of the nanofiber alignment efficiency by SEM counting (Figure 1c) revealed successful orthogonal and parallel alignment to the stretch axis with 80% of the fibers contained within ±15° (Figure 1c and Figure S5e, Supporting Information). In contrast, for the randomly oriented layers, a uniform distribution of directions was observed (Figure 1d and Figure S5f, Supporting Information).

The feasibility of exploiting the morphological variations between these nanofiber layers to achieve a tailored wetting state, hereinafter referred to as static tuning (prestretch), was assessed with respect to a range of prestretch and alignment parameters. Static tuning of the films' wetting properties was possible only with the parallel-aligned wave-like films (**Figure 2**a,b). Owing to the impact of anisotropicity on the film wetting properties,[32,33] the contact angles of the nanofibrous films were imaged from two orthogonal viewpoints, parallel and perpendicular to the fibers alignment (Figure S6, Supporting Information). The largest variations in contact angles were 6.23° (Figure S6a, Supporting Information) and occurred for the straight fibers (orthogonally alignment) films with 100% prestretch. In contrast, the wave-like fibers, obtained by
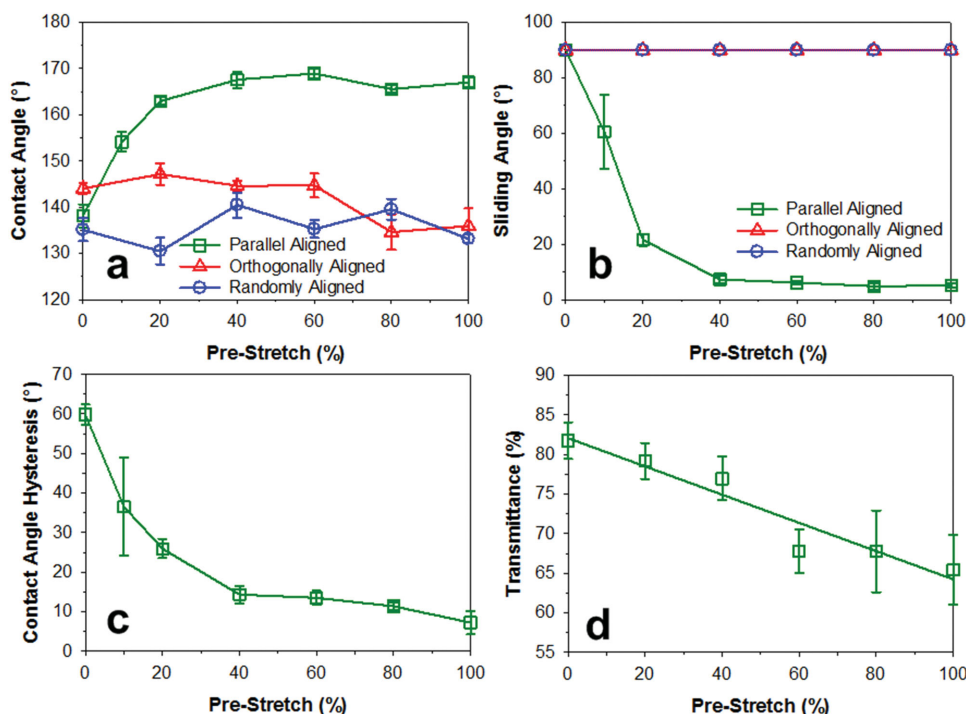


**Figure 2.** a) Contact angles and b) sliding angles as a function of the stretch ratio for parallel (green), orthogonally (red), and randomly aligned (blue) nanofiber layers on elastic PDMS substrates. c) Contact angle hysteresis for parallel-aligned nanofiber layers as a function of the prestretch ratio. d) UV–vis transmittance at λ = 600 nm for the parallel-aligned nanofibers as a function of their prestretch.

parallel-alignment, had negligible anisotropicity with contact angle variations smaller than <1° for an imaging angle of 0° and 90° to the fiber alignment (Figure S6b, Supporting Information). This is tentatively attributed to their Cassie–Baxter wetting state that limits the interaction of the solid substrate texture with the liquid droplet. These variations were well within the standard batch-to-batch contact angle variations (1°–5°) of these films, and thus further contact angles during dynamic tuning were reported for an imaging direction of 90° to the fiber alignment only. For these films, increasing the pre-stretch from 0% to 100% increased the water contact angle (CA) from 138° to 167° (Figure 2a) and decreased the sliding angle (SA) from 90° (pinning) to 5° (Figure 2b). Even with very mild prestretch ratios of 10% and 20%, these films transited from adhesive hydrophobic of the unstretched films to lotus leaf-like repulsive superhydrophobicity. With a moderate prestretch of 40%, stable repulsive superhydrophobicity was achieved resulting in static CAs in excess of 160° (Figure 2a), and SAs below 10° (Figure 2b) already for microdroplets of 5 µL. This demonstrates, for the first time, that low SA, repulsive super-hydrophobicity can be achieved by a wave-like nanofiber morphology offering a facile scalable approach for the rapid (1 min) fabrication of water-impenetrable superhydrophobic surfaces. An advantage of this ultraporous morphology is that super-hydrophobicity is achievable with low uniaxial strain while state-of-the-art 2D films morphologies commonly require relatively high biaxial strains.[5] This is attributed to the secondary degree of nanoscaled hierarchy achieved by in-plane curling of 1D nanostructures. In contrast, random and orthogonally aligned nanofibers did not transit wetting states and preserved their initial adhesive hydrophobic properties (Figure 2a,b). Primarily, orthogonally aligned fiber films did not form a wave-like morphology and thus could not undergo the wave-to-straight shapeshifting necessary for Cassie–Baxter to Wenzel transition. Similarly, the randomly aligned fiber films had mostly straight fibers and only few wave-like fibers, and thus were not able to impart a transition of wetting states at the macroscale.

The statically tuned wetting properties of the optimal parallel-aligned wave-like nanofibers were further characterized by contact angle hysteresis (CAH). The CAH dropped steeply from 60° to 15° with increasing prestretch from 0% to 40%, in good agreement with the CA and SA analysis (Figure 2c). At 100% prestretch, a CAH of 7° was achieved. These results further indicate that, as soon as a slight wave-like curvature is obtained (e.g., at 20% prestretch), the nanofiber layer becomes impenetrable to water. Based on these observations, the static tunable wetting state of these nanofiber layers is attributed to a transition from dewetting Cassie–Baxter to the wetting Wenzel state through the Cassie-impregnating regime. UV–vis analysis of the parallel-aligned nanofibers revealed a linear decrease in transmittance from 85% to 65% with increasing prestretch from 0% to 100% (Figure 2d). This is tentatively attributed to the formation of periodic microscale light-scattering structures and is in line with the fiber morphology observed by SEM.

To assess the feasibility of fabricating surfaces with continuously and reversibly tunable wettability, hereinafter referred to as dynamic tuning (straining), the wave-like nanofiber films were dynamically strained and their wetting properties were simultaneously monitored. The 40% prestretched wave-like

nanofibers were selected as the most promising morphology. In fact, while achieving the same robust repulsive superhydrophobicity of the 100% prestretched samples, the larger wavelengths and smaller in-built stress of the former were beneficial in obtaining reversible deformation of the fiber shape. In addition to the 100% prestretched samples, the unstretched (0%) parallel-aligned nanofibers were also tested as a control sample. For the latter, wetting analysis revealed negligible variations of the CA during dynamic straining of the PDMS substrates, resulting always in hydrophobic surfaces (**Figure 3**a, blue line). In contrast, the 40% and 100% prestretched films had gradually decreasing CAs with increasing dynamic strain (Figure 3a, green and red lines). Surprisingly, the transition to nonsuperhydrophobic CAs occurred for the 40% prestretched films only at a relatively high dynamic strain of 80% (Figure 3a, green line) while for the 100% prestretched films, superhydrophobic CAs were maintained even up to 100% dynamic strain (Figure 3a, red line). These results are indicative of a certain degree of morphological hysteresis in the stretching cycle.

The SA and CAH analysis during dynamic strain revealed further insights on the properties of these tunable surfaces. No transitional behavior was detected for the 0% prestretched films independently of the applied dynamic strain, with SAs and CAHs being within those reported for rose petal-like adhesive hydrophobicity regimes[34] (Figure 3b). A distinctive transitional behavior was found for the 40% prestretched films, with the SA switching from repulsive superhydrophobicity to adhesive superhydrophobic droplet pinning (Figure 3c) at a dynamic strain of 40%. A similar transitional behavior was achieved with the 100% prestretched developed films, however, with the SA switching from lotus to rose-like only approaching a dynamic strain of 100% (Figure 3d). In good agreement with the SA analysis, the CAH of the 40% and 100% prestretched films approached the adhesive (rose petal) superhydrophobic region of 50°–60° at a dynamic strain of 40% and 100%, respectively. For the 40% prestretched films, this was characterized by a sharp step increase of 38° in CAH with increasing dynamic strain from 20% to 40%. In contrast, the unstretched samples had the highest CAH of 83° resulting in robustly pinned microdroplets independently of the applied dynamic strain. These findings indicate that the 40% prestretched parallel-aligned nanofiber layers, hereinafter referred to as the optimal films, and a dynamic strain between 20% to 40% hold the highest potential for fabrication of dynamically switchable water adhesive-repulsive surfaces (Figure 3c). This strain-tunable surface wetting was attributed to the 2D to 1D morphological transformation (**Figure 4**a–c) of the wave-like nanofibers during their straightening. This is, notably different from the traditional wrinkling and buckling of flat dense films where a 3D to 2D transformation is imposed.[5,29]

The 2D to 1D nanofiber dynamic and wetting mechanism were investigated by optical analysis of a complete strain–relaxation cycle (Figure 4d). A video of the nanofiber morphological response to strain and subsequent relaxation is presented in the Supporting Information (Video M1). In their relaxed morphology, the optimal films form a series of air gaps trapped within the bendings of the wave-like nanofiber layers that result in a Cassie–Baxter state with a lotus-like water-impenetrable surface (Figure 4b,c). During dynamic strain, the bending
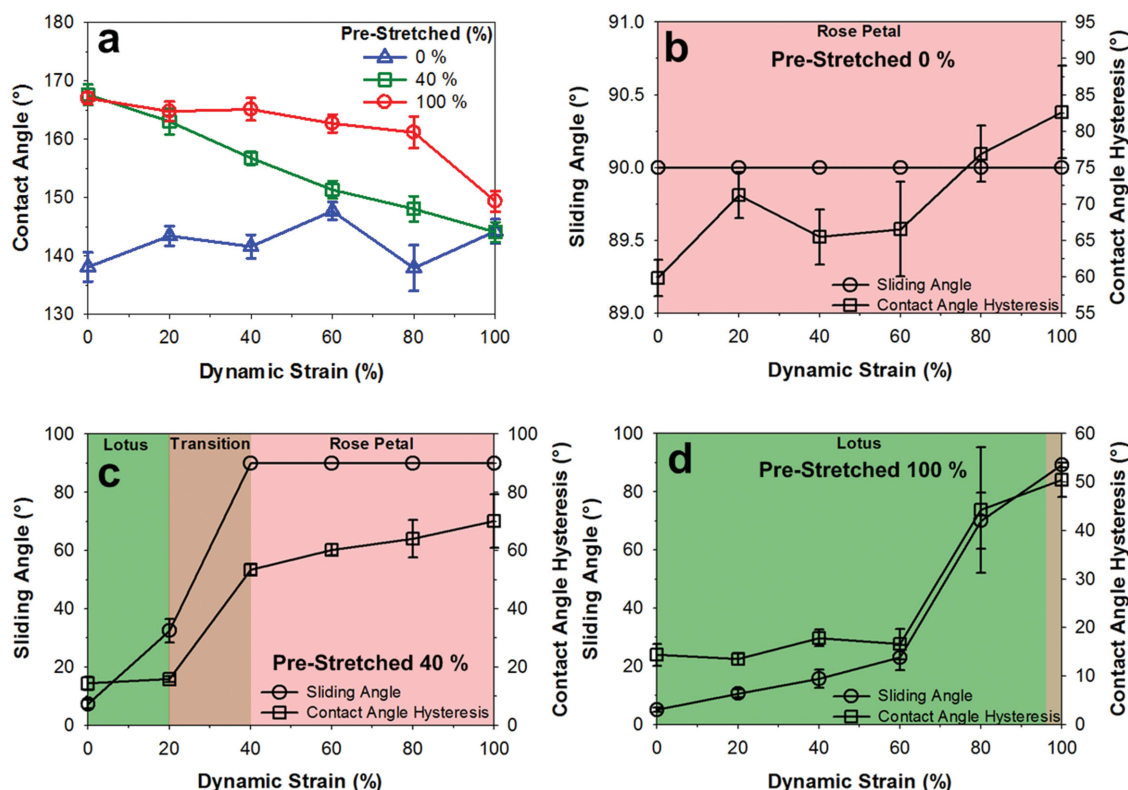
www.MaterialsViews.com

ADVANCED
FUNCTIONAL
MATERIALS
www.afm-journal.de

FULL PAPER

**Figure 3.** Variation of a) contact angles, b–d) sliding angles (left axis) and contact angle hysteresis (right axis) of the 0%, 40%, and 100% prestretched films. Note that there is no wetting state transition for the films with 0% and 100% prestretch, while a distinctive wetting transition is achieved for the surface of the 40% prestretched films.

of the wave-like nanofiber is lost (Figure 4c) enabling release of the trapped air. The change in film morphology was also investigated by WLI (Figure S7, Supporting Information) that revealed an average drop in film thickness of 500 nm with increasing strain from 0% to 40%. This results in a transition from Cassie–Baxter to impregnated Cassie state and, for small prestretch, even to Wenzel wetting. This model matches well with the superhydrophobic water droplet pinning (Figure 3c) observed for the 40% strained optimal films.

The optimal films were tested for passive and active microdroplet manipulation. As determined above, optimal superhydrophobic adhesion was exhibited with a dynamic strain of 20%–40%. Importantly, applying a dynamic strain below the original prestretch helped to maintain the nanofiber integrity. Passive droplet control was first demonstrated by dynamically switching of the surface's wettability from a repulsive (**Figure 5**a) to an adhesive hand (Figure 5b). At a strain ratio of 30%, it was possible to pick up a 6 μL droplet. In addition, an active responsive mechanical hand was achieved, demonstrating the feasibility of continuous microdroplet droplet capture, manipulation, and controlled release. This was readily achieved by dynamically straining the backside of the PDMS substrate with a tipped probe of 1 mm in diameter. The probe stretched the elastomeric PDMS film radially during the downward motion. This was set to encounter a 6 μL microdroplet placed at 10 mm distance from the PDMS substrate. The microdroplet was then lifted from the superhydrophobic surface on which it was previously placed. Thereafter, recontraction of

the adhesive rose petal-like surface during the upward motion, first vertically displaced the droplet and thereafter continuously increased the CA eventually resulting in a repulsive lotus-like surface and droplet release by breakage of the residual capillary bridge (Figure 5c and Video M2, Supporting Information). In this work, the largest droplet size held in the adhesive rose petal state was 10 μL, which is in line with previous studies.[34] The smallest droplet size captured and released was 3 μL. The small pore sizes of these films (5–6 μm) suggest that it should be possible to manipulate droplet sizes significantly smaller than 3 μL. The maximum droplet volume captured and released, here, was 6 μL.

Cyclic dynamic switching from an adhesive to a repulsive wetting state was demonstrated with the optimal films by periodic application of 30% dynamic strain and relaxation (**Figure 6**a,b). Analysis of the reversibility was performed with a series of 10 wetting cycles. The SAs were consistently tuned from pinned 90° to less than 10° between each cycle (Figure 6a). Advancing, receding contact angles (Figure S2c, Supporting Information) and CAH (Figure 6b) further confirmed the switchable adhesive-repulsive states of the optimized films. Upon 30% dynamic strain, consistently high CAHs of 50°–60° were maintained that are characteristics of adhesive rose petal-like surfaces[34] (Figure 6b). Upon relaxation, consistently low CAHs of between 10° and 20° were recovered, indicating a repulsive lotus leaf-like wetting state (Figure 6b). SEM characterization of the post-cycled films (Figure S2b, Supporting Information) revealed that the nanofibers and the layers
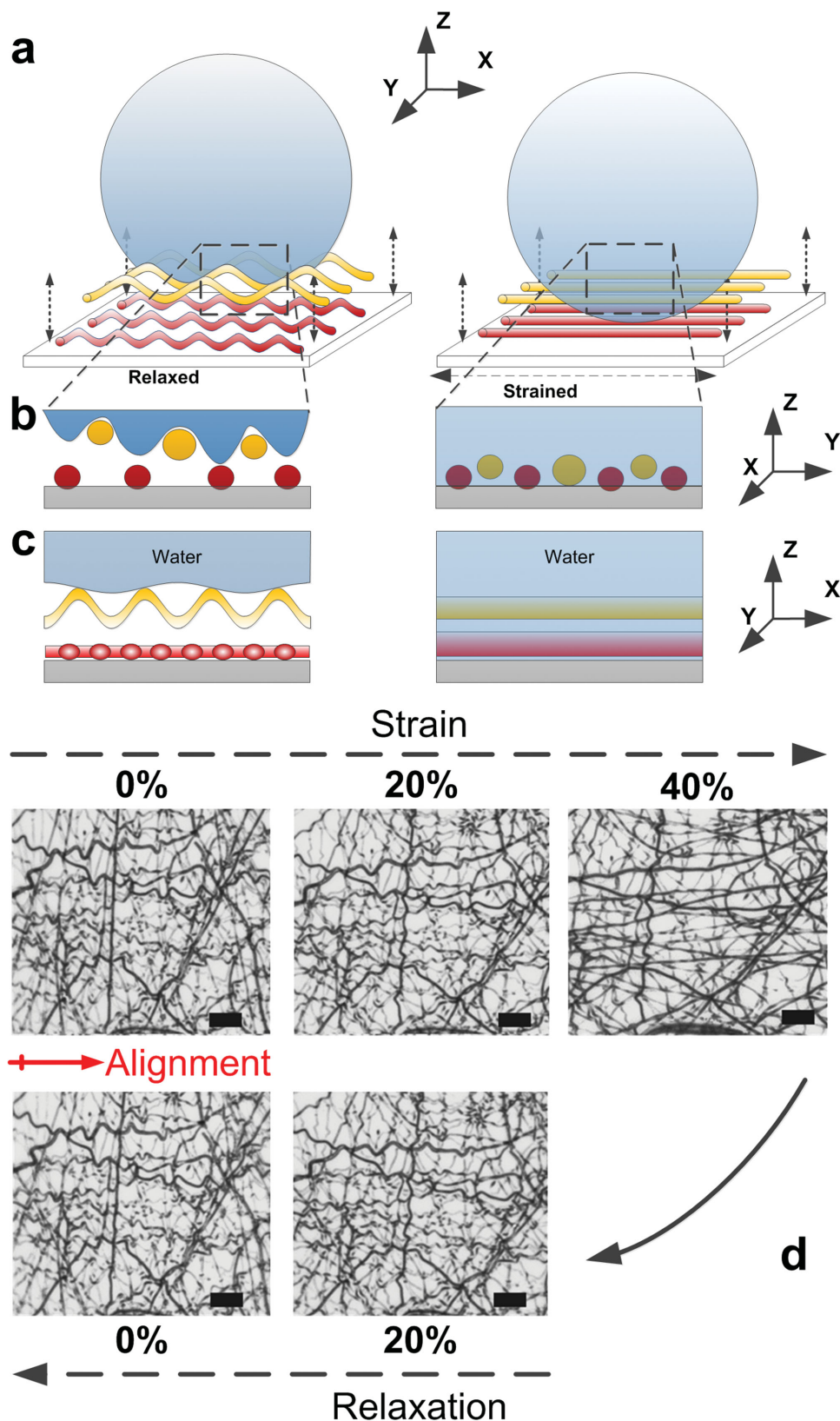
**Figure 4.** a) Schematic drawing describing the dynamic switching mechanism between Cassie–Baxter lotus-like to the Wenzel penetrated states through b,c) strain-induced straightening of in-plane and out-of-plane wave-like nanofibers. The strain of the wave-like nanofibers results in the release of the air gaps trapped within the bendings. d) In situ optical microscope images displaying a full strain–relaxation cycle. The scale bar is 10 μm.
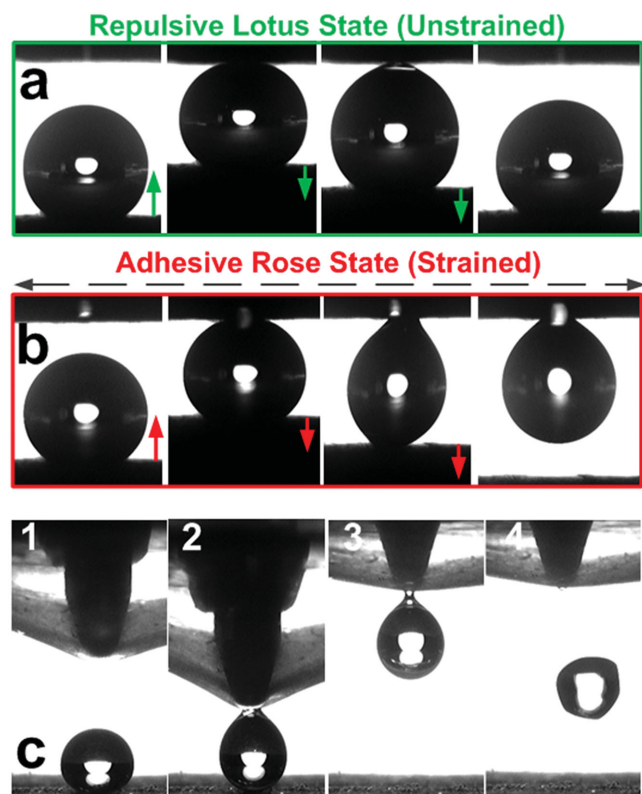
**Figure 5.** Dynamic tuning of surface wetting by dynamic straining of the parallel-aligned nanofiber layers (40% prestretched). Mild uniaxial straining from 0% to 30% enables switchable a) repulsive to b) adhesive superhydrophobic states. Demonstration of mechanical hand-like droplet manipulation by c) lift-off (2–3) of a 6 µL droplet and its controlled release (4).



**Figure 6.** Cyclic switching of repulsive to adhesive superhydrophobic wetting state by application of uniaxial dynamic strain of 30% and relaxation showing fully reversible a) sliding angles and b) contact angle hysteresis.

preserved their morphological integrity with no observable material cracks, fracture and discernable morphological variations from the as-prepared samples (Figure S2a, Supporting Information). These results demonstrate the complete reversibility of the wetting and structural properties switch despite the crystalline nature of polystyrene, showcasing the robustness of this tunable surface texture.

## 3. Conclusions

A novel surface texture capable of static and dynamic reversible switching of its wetting state from adhesive to highly repulsive superhydrophobicity was developed by a facile and scalable bottom-up approach. Unprecedentedly, we have demonstrated that the strain-induced transformation of 2D wave-like nanofibers into a 1D straight morphology can be exploited to achieve a transition from Cassie–Baxter to the Cassie-impregnating and Wenzel wetting states. This was achieved by dynamic strain engineering of a bilayer morphology composed of a functional ultraporous film of wave-like nanofibers on an elastic support. Multicycle mechanically actuated tuning of the SAs and CAHs from 8° to 90° (pinned) and 15° to 55°, respectively, was achieved by low uniaxial dynamic strain of 30%. Optimal films were able to perform dynamic mechanical hand-like manipulation of water droplets demonstrating lift-off,
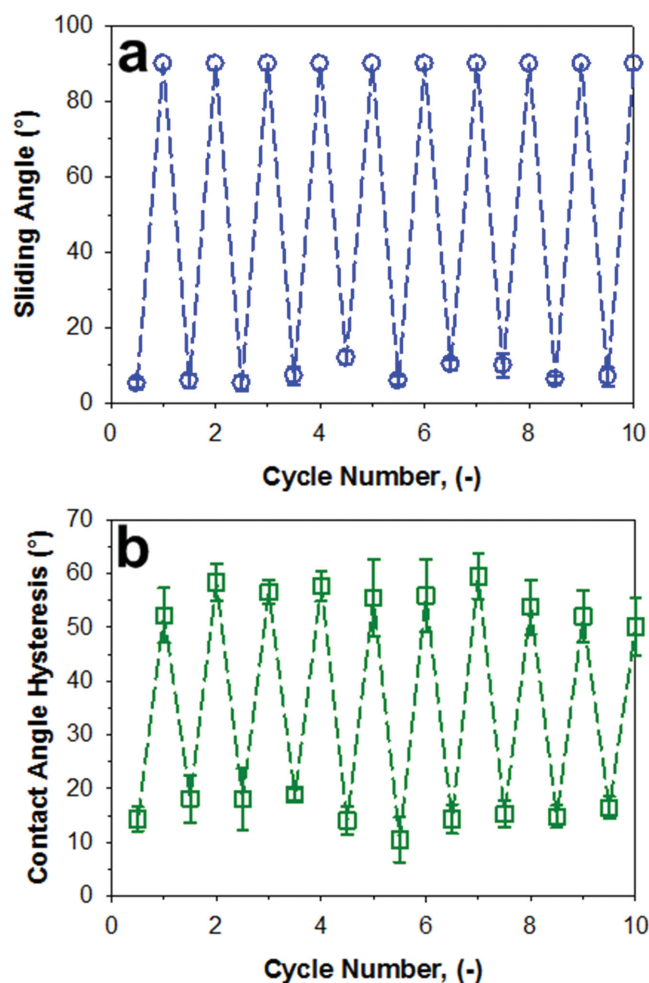
manipulation and controlled-release of up to 6 µL microdroplets by a simple pin-actuated radial stretch of the PDMS substrate. This highly performing bilayer structure has direct application in droplet control systems[8,35] and microreactor arrays.[36] Furthermore, it is a low-cost and scalable design that offers a flexible platform for fabrication of smart interfaces with numerous other applications including dynamically tunable membrane technology,[24] water harvesting and purification,[37] flexible electronics,[19] and biosensors.[38]

## 4. Experimental Section

*Polymer Solution Preparation*: Polystyrene (Sigma-Aldrich, $M_w = 280\,000$) (PS) solutions were made by dissolving 0.944 g of PS in 10 mL of *N,N*-dimethyl formamide (Sigma-Aldrich, anhydrous, ≥99.8%) (DMF). Dodecyl trimethyl ammonium bromide (Sigma-Aldrich, ≥98%) (DTAB) was added at to the PS solution at concentrations of 1.9 mg mL$^{-1}$.

*Substrate Preparation*: Polydimethylsiloxane (silicone) substrates were prepared using Sylgard 184 (Dow Corning), which comprises of a 10:1 ratio of base elastomer to curing agent. These were mixed vigorously together, casted on petri dishes and degassed for 30 min

**FULL PAPER**

before a thermal curing procedure at 70 °C for 50 min. Surface energies of the bare PDMS surface was computed through a 5 point contact angle analysis (Figure S8, Supporting Information) at 119 ± 1.3°. Casted PDMS slides possessed a thickness of 0.5 mm and dimensions were crafted so as to suit substrates for electrospinning (Figure S1b, Supporting Information).

*Electrospinning*: Electrospinning of the PS nanofibrous layer on PDMS was developed using a vertical electrospinning setup (Electrospunra ES210, Singapore), at a working distance and flow rate of 10 cm and 1.0 mL h$^{-1}$ with an applied voltage of 30 kV for 1 min between 35% and 45% relative humidity. A travel distance of 7 cm with a speed of 2 cm s$^{-1}$ was used to improve homogeneity. Copper masks were crafted to provide a charge collection zone with dimensions of 2.5 × 2.5 cm. Alignment was promoted by modification of the mask through selective insulation using polypropylene sheets. Substrates were uniaxially prestretched and calibrated between 0% and 100% strain prior to deposition. The stretch of the substrate during fiber deposition is referred as "prestretch." After electrospinning, the copper mask was gently removed while pressing the nanofiber film against the PDMS substrate with a square stamp of 2.5 × 2.5 cm. The PDMS substrate was thereafter relaxed, completing the synthesis of the nanofiber coatings (Figure S1e, Supporting Information). Samples were not moisture sensitive and could be stored indefinitely without losses in functionality. The two types of fibers were classified by the orientation of their longitudinal axes with in-plane fibers having longitudinal axes parallel to the substrate and out-of-plane fibers having longitudinal axes that are partially vertical to the substrate.

*Wetting Analysis*: Films collected were stored overnight to facilitate the completion of solvent evaporation prior to further testing. Wetting analysis was conducted within 48 h of synthesis. Owing to the impact of anisotropicity on the film wetting properties,[32,33] the contact angles of the orthogonally and parallel-aligned nanofibrous films were imaged (Figure S6, Supporting Information) from different orientations (0° and 90°) to the fiber alignment and assessed for variations. The CA variations (Figure S6, Supporting Information) were well within the standard batch-to-batch contact angle variations (1°–9°) of both orthogonally and parallel-aligned nanofibrous films, and further contact angles during dynamic tuning were thus reported for an imaging direction of 90° to the fiber alignment only. The static water contact angle (CA) was measured by placing and averaging six drops of deionized water (5 µL) on sample surfaces produced across batches. The sliding angle (SA) was determined by placing a 5 µL drop of deionized water directly on sample surfaces prior to tilting via an optical or mechanical goniometer. Results were averaged across six readings. The contact angle hysteresis (CAH) was measured via the drop-in drop-out (DIDO) technique (1–9 µL, three readings), which involves subtraction of the receding contact angle from the advancing contact angle. The former was measured at 1 µL while the latter was measured at 9 µL. Data were presented as mean ± standard errors (CA, SA and CAH). Parameters were collected for both statically and dynamically tuned films. The dynamic tuning of the wetting properties of the nanofiber films by applying a strain is referred as "strain". A fresh droplet is placed each time on the dynamically strained films between further straining or relaxing the interface during CA, SA and CAH measurements. Dynamic and static images were recorded using a KSV CAM200 contact angle goniometer (Finland) with a heliopan ES43 camera (Japan). Whenever possible, the CA, SA and CAH were computed by a commercially available (CAM2008) program. All substrate extension and relaxation were conducted at approximately 0.625 mm s$^{-1}$ using a custom-built electrically operated stretch apparatus.

*Surface Analysis*: Morphological optimizations were first conducted using a light microscope (Nikon Eclipse E200, TV lens 0.55× DS) on coated PDMS substrates. These optimization experiments were conducted four times to ensure repeatability. Samples were then analyzed via scanning electron microscopy (Zeiss UltraPlus analytical scanning electron microscope (FESEM) at 3 kV). Prior to examination, SEM specimens were platinum sputter-coated for 2 min at 20 mA. Average fiber dimension was analyzed via ImageJ using 50 counts of each nanostructure. Data was presented as mean ± standard deviations.

Fiber alignment was determined via observing SEM images (4.4k and 8.8k magnifications) of straight aligned fibers (five separate cross-batch samples), with between 60 and 100 counts per sample made on aligned and misaligned fibers. Statistical histogram analysis was thus computed through 300 fiber counts with standard errors analyzed through five batches for each type of nanofiber films (aligned or random). Wavelengths of in-plane waveformed fibers were determined based on 1–4 consecutive waves with at least 10 counts. Surface coverage was determined through ImageJ using SEMs based on optimizing contrast, enabling the estimation of fibrous domains through six cross-batch samples. Data was presented as mean ± standard deviations. UV–vis analysis was conducted using a microplate reader (Tecan 200 PRO, Switzerland) from 300 to 800 nm with 10 scans per cycle. Data was presented as mean ± standard errors. In situ optical analysis: The in situ optical analysis was performed with a Leica microscope (DM2700M) equipped with a long working distance 50× nosepiece and custom-made microscope-compatible stretching stage with 5 µm displacement accuracy. 3D optical profiler measurements were performed with the Bruker Contour GT-K with a 50× lens and a 2× multiplier. VXI acquisition mode was used in conjunction with a custom made stretching stage with 5 µm displacement accuracy.

## Supporting Information

Supporting Information is available from the Wiley Online Library or from the author.

## Acknowledgements

[1] A. R. Wheeler, *Science* **2008**, *322*, 539.
[2] T. Zhu, C. Cai, C. Duan, S. Zhai, S. Liang, Y. Jin, N. Zhao, J. Xu, *ACS Appl. Mater. Interfaces* **2015**, *7*, 13996.
[3] X. Yao, Y. Hu, A. Grinthal, T.-S. Wong, L. Mahadevan, J. Aizenberg, *Nat. Mater.* **2013**, *12*, 529.
[4] Y. Si, Q. Fu, X. Wang, J. Zhu, J. Yu, G. Sun, B. Ding, *ACS Nano* **2015**, *9*, 3791.
[5] C. Cao, H. F. Chan, J. Zang, K. W. Leong, X. Zhao, *Adv. Mater.* **2014**, *26*, 1763.
[6] Z. Wang, L. Ci, L. Chen, S. Nayak, P. M. Ajayan, N. Koratkar, *Nano Lett.* **2007**, *7*, 697.
[7] D. J. Babu, S. N. Varanakkottu, A. Eifert, D. de Koning, G. Cherkashinin, S. Hardt, J. J. Schneider, *Adv. Mater. Interfaces* **2014**, *1*, 1300049.

www.MaterialsViews.com

ADVANCED
FUNCTIONAL
MATERIALS
www.afm-journal.de

FULL PAPER

[8] D. Wu, S. Z. Wu, Q. D. Chen, Y. L. Zhang, J. Yao, X. Yao, L. G. Niu, J. N. Wang, L. Jiang, H. B. Sun, *Adv. Mater.* **2011**, *23*, 545.

[9] Z. Han, B. Tay, C. Tan, M. Shakerzadeh, K. Ostrikov, *ACS Nano* **2009**, *3*, 3031.

[10] B. Kakade, R. Mehta, A. Durge, S. Kulkarni, V. Pillai, *Nano Lett.* **2008**, *8*, 2693.

[11] J. Rafiee, M. A. Rafiee, Z.-Z. Yu, N. Koratkar, *Adv. Mater.* **2010**, *22*, 2151.

[12] F. Mumm, A. T. J. van Helvoort, P. Sikorski, *ACS Nano* **2009**, *3*, 2647.

[13] Q. Cheng, M. Li, Y. Zheng, B. Su, S. Wang, L. Jiang, *Soft Matter* **2011**, *7*, 5948.

[14] N. Verplanck, E. Galopin, J.-C. Camart, V. Thomy, Y. Coffinier, R. Boukherroub, *Nano Lett.* **2007**, *7*, 813.

[15] K. Efimenko, M. Rackaitis, E. Manias, A. Vaziri, L. Mahadevan, J. Genzer, *Nat. Mater.* **2005**, *4*, 293.

[16] P. K. Byrne, C. Klimczak, A. M. Celal Sengor, S. C. Solomon, T. R. Watters, I. I. S. A. Hauck, *Nat. Geosci.* **2014**, *7*, 301.

[17] C. F. Guo, V. Nayyar, Z. Zhang, Y. Chen, J. Miao, R. Huang, Q. Liu, *Adv. Mater.* **2012**, *24*, 3010.

[18] J. Y. Chung, T. Q. Chastek, M. J. Fasolka, H. W. Ro, C. M. Stafford, *ACS Nano* **2009**, *3*, 844.

[19] Y. Duan, Y. Huang, Z. Yin, N. Bu, W. Dong, *Nanoscale* **2014**, *6*, 3289.

[20] R. J. Hamers, *Nature* **2001**, *412*, 489.

[21] S. Xu, Z. Yan, K.-I. Jang, W. Huang, H. Fu, J. Kim, Z. Wei, M. Flavin, J. McCracken, R. Wang, A. Badea, Y. Liu, D. Xiao, G. Zhou, J. Lee, H. U. Chung, H. Cheng, W. Ren, A. Banks, X. Li, U. Paik, R. G. Nuzzo, Y. Huang, Y. Zhang, J. A. Rogers, *Science* **2015**, *347*, 154.

[22] Y. H. Kim, Y. M. Lee, J. Y. Lee, M. J. Ko, P. J. Yoo, *ACS Nano* **2012**, *6*, 1082.

[23] A. K. Epstein, D. Hong, P. Kim, J. Aizenberg, *New J. Phys.* **2013**, *15*, 095018.

[24] S. J. Cho, H. Nam, H. Ryu, G. Lim, *Adv. Funct. Mater.* **2013**, *23*, 5577.

[25] J. Y. Sun, S. Xia, M. W. Moon, K. H. Oh, K. S. Kim, *Proc. R. Soc. A* **2011**, *468*, 932.

[26] D. Kim, D. Jung, J. H. Yoo, Y. Lee, W. Choi, G. S. Lee, K. Yoo, J.-B. Lee, *J. Micromech. Microeng.* **2014**, *24*, 055018.

[27] J. Zang, S. Ryu, N. Pugno, Q. Wang, Q. Tu, M. J. Buehler, X. Zhao, *Nat. Mater.* **2013**, *12*, 321.

[28] Y. C. Chen, A. J. Crosby, *Adv. Mater.* **2014**, *26*, 5626.

[29] J. S. Choi, Y. Piao, T. S. Seo, *Biotechnol. Bioprocess Eng.* **2014**, *19*, 269.

[30] J. Lin, Y. Cai, X. Wang, B. Ding, J. Yu, M. Wang, *Nanoscale* **2011**, *3*, 1258.

[31] Y. Miyauchi, B. Ding, S. Shiratori, *Nanotechnology* **2006**, *17*, 5151.

[32] N. Kashaninejad, W. K. Chan, N.-T. Nguyen, *Langmuir* **2012**, *28*, 4793.

[33] N. Kashaninejad, N.-T. Nguyen, W. K. Chan, *Soft Matter* **2013**, *9*, 527.

[34] W. S. Y. Wong, N. Nasiri, G. Liu, N. Rumsey-Hill, V. S. J. Craig, D. R. Nisbet, A. Tricoli, *Adv. Mater. Interfaces* **2015**, *2*, 1500071.

[35] B. A. Kakade, *Nanoscale* **2013**, *5*, 7011.

[36] W. H. Chong, L. K. Chin, R. L. Tan, H. Wang, A. Q. Liu, H. Chen, *Angew. Chem. Int. Ed.* **2013**, *52*, 8570.

[37] H. Zhou, H. Wang, H. Niu, T. Lin, *Sci. Rep.* **2013**, *3*, 2964.

[38] P. K. Chow, E. Singh, B. C. Viana, J. Gao, J. Luo, J. Li, Z. Lin, A. L. Elías, Y. Shi, Z. Wang, M. Terrones, N. Koratkar, *ACS Nano* **2015**, *9*, 3023.